Tyler Hague NUCLEAR PHYSICS

SUPER AWESOME MARATHON THESIS (pp.)

Director of Thesis/Dissertation: MK MP

This is the abstract file abstract.tex

My research field is experimental nuclear physics. My work was ——

We present the details of the analysis, the obtained distributions, and their discussion.

MARATHON is a Deep Inelastic Scattering experiment in Jefferson Lab's Hall A. The experiment utilized Deuterium, Helium-3, and Tritium targets to extract the F_2^n/F_2^p structure function ratio and R. **Need to give an explanation of R. Talk about EMC and why we're looking at these things. Mention uniqueness of having Tritium target**

SUPER AWESOME MARATHON THESIS

A thesis /dissertation submitted to
Kent State University in partial
fulfillment of the requirements for the
degree of Master of Science / Doctor of Philosophy

by

Tyler Hague

November, 2016

Thesis/ Dissertation written by

Tyler Hague

B.S., Abilene Christian University, 2012

M.S/ Ph.D., Kent State University, TBD

Approved by

_____, Chair, Masters Thesis/ Doctoral Dissertation Committee

_____, Members, Masters Thesis/Doctoral Dissertation Committee

_____ ,

_____ ,

_____ ,

Accepted by

_____ , Chair, Department of Physics

_____ , Dean, College of Arts and Sciences

Table of Contents

List of Figures

List of Tables

Acknowledgments

This is the acknowledgements text.

Chapter 1

Introduction

As I chose a starting point for writing, this has become more of a theory chapter. It will likely be renamed and renumbered to reflect that soon.

1.1 The Quark-Parton Model

- Decide how "historical" to be
- Hadrons are composed of quarks
- Quarks are bound by gluons (strong force)
- Gluons create the "sea" via $g \to q\bar{q} \to g$
- Electric and Magnetic form factors?

The Quark-Parton Model describes the composition of hadrons, both baryons and mesons. Prior to 1964, it was believed that hadrons were as small as it got. However, the adherence of hadrons to the eight-fold way, a categorization of hadrons by charge and strangeness, suggested that there was some underlying mechanism that had yet to be discovered.

In 1964, Gell-Mann and Zweig independently suggested that hadrons could be composed smaller elementary particles. Gell-Mann offered the name "quarks" for these constituents.

Furthering the theory, in Novemeber 1974 two separate experiments published the discovery of the (now named) J/ψ particle. The long lifetime of the J/ψ suggested that new physics must be at play. The Quark-Parton Model predicted the existence of a quark symmetric to the strange quark, called the charm quark. It was determined that the J/ψ could be a meson comprised of a charm and anti-charm, suggesting the validity of the model.

1.2 Deep Inelastic Scattering

How does it work? Electron comes in, exchanges photon with nucleon. Boom.

At its most basic, Deep Inelastic Scattering (DIS) is the scattering of a lepton from a nucleon. The two participants exchange a virtual boson, the lepton scatters, and the nucleon is excited to a hadronic final state X with higher mass.

$$\ell + N \rightarrow \ell' + X$$

For the MARATHON experiment we will focus on electromagnetic DIS. In this case the lepton is charged and the exchanged virtual boson is a virtual photon. The JLab CEBAF accelerator provides an electron beam, so from here on the lepton will be written as an electron.

$$e^- + N \rightarrow e^- + X$$

PUT DIS FEYNMAN DIAGRAM HERE

By interacting with a single nucleon, DIS is a powerful tool for studying nucleon structure. By looking at the DIS cross section, we can see how the nuclear structure functions readily present themselves.

If we assume Lorentz invariance, **P** and **T** invariance, and conservation or lepton current, the cross section is

$$\frac{d^2\sigma}{d\Omega dE'} = \frac{\alpha^2}{Q^4}\frac{E'}{E}L^{(s)^{\mu\nu}}W^{(s)}_{\mu\nu} \tag{1.1}$$

where Q^2 is the 4-momentum transfer, E is the beam energy, E' is the scattered electron energy, $L^{(s)^{\mu\nu}}$ is the lepton tensor, and $W^{(s)}_{\mu\nu}$ is the symmetric hadronic tensor.

When written explicitly in the laboratory frame, we arrive at

DIS Cross Section

(1.2)

$$\sigma \equiv \frac{d^2\sigma}{d\Omega dE'}\left(E, E', \theta\right) = \frac{4\alpha^2\left(E'\right)}{Q^4}\cos^2\left(\frac{\theta}{2}\right)\left[\frac{F_2\left(\nu, Q^2\right)}{\nu} + \frac{2F_1\left(\nu, Q^2\right)}{M}\tan^2\left(\frac{\theta}{2}\right)\right]$$

1.3 F_2 Structure Functions

"These two form factors, $F_{1,2}(q^2)$, parametrize our ignorance of the detailed structure of the proton". [9]

TALK MORE ABOUT THIS RELATION

The following relation allows the cross section to be written in terms of F_2 only.

$$F_1 = \frac{F_2\left(1 + Q^2/\nu^2\right)}{2x\left(1 + R\right)} \tag{1.3}$$

Here x is the bjorken scaling variable and R is the ratio of the longitudinal cross section to the transverse cross section, σ_L/σ_T.

Plugging this in we arrive at

$$\frac{d^2\sigma}{d\Omega dE'}\left(E, E', \theta\right) = \frac{4\alpha^2\left(E'\right)}{Q^4}\cos^2\left(\frac{\theta}{2}\right)F_2\left[\frac{1}{\nu} + \frac{\left(1 + Q^2/\nu^2\right)}{xM\left(1 + R\right)}\tan^2\left(\frac{\theta}{2}\right)\right] \tag{1.4}$$

1.4 $R = \sigma_L/\sigma_T$

$R = \sigma_L/\sigma_T$. R is independent of atomic number. This facilitates us taking ratios

If we instead approach DIS as the production and absorption of a virtual photon we can extract a different structure function $R = \sigma_L/\sigma_T$. That is, the ratio of the cross sections for absorbing longitudinal photons to transverse photons.

We can write the DIS cross section in terms of these cross sections as

$$\frac{d^2\sigma}{d\Omega dE'}(E, E', \theta) = \Gamma\left[\sigma_T\left(x, Q^2\right) + \epsilon\sigma_L\left(x, Q^2\right)\right] \tag{1.5}$$

In this equation Γ is the flux of transverse virtual photons and ϵ is the relative flux of longitudinal virtual photons. These are defined by

$$\Gamma = \frac{\alpha K E'}{2\pi^2 Q^2 E_0 (1-\epsilon)} \tag{1.6}$$

$$\epsilon = \frac{1}{1 + 2\left(1 + \nu^2/Q^2\right)\tan^2\left(\frac{\theta}{2}\right)} \tag{1.7}$$

Here, K is the laboratory photon energy

$$K = \frac{W^2 - M^2}{2M} \tag{1.8}$$

1.5 EMC Ratios

Looking at the EMC-type ratios for Helium-3 and Tritium make it clear that we can extract the nucleon structure function ratio from the nuclear

structure function ratio. We will use a calculation of the super ratio to do this extraction.

Chapter 2

The Experiment

2.1 The Measurement

2.1.1 What are we measuring

2.1.2 How are we measuring it

2.1.3 Run Plan

2.2 The Apparatus

2.2.1 Hall A HRS Spectrometers

2.2.2 CEBAF Accelerator

2.3 Beamline Components

The Hall A Beamline has several measurement devices that allow the experimenter to fully understand the beam that is being delivered to the hall. For positioning, there are the Beam Position Monitors and the Harp. For beamspot sizing, there is the raster. For current and charge measurements, there are the Beam Current Monitors.

2.3.1 Beam Position Monitors

The Beam Position Monitors (BPMs) are a pair of measurement devices that consist of four sensing wires. By calibrating the signal received from each wire, the experimenter can reconstruct the position of the beam as it passed the BPM. Using both BPMs in conjunction allows the experimenter to determine the beam trajectory and where the electrons are incident on the target.

The BPMs are calibrated using a Harp fork. The Harp consists of three wires that

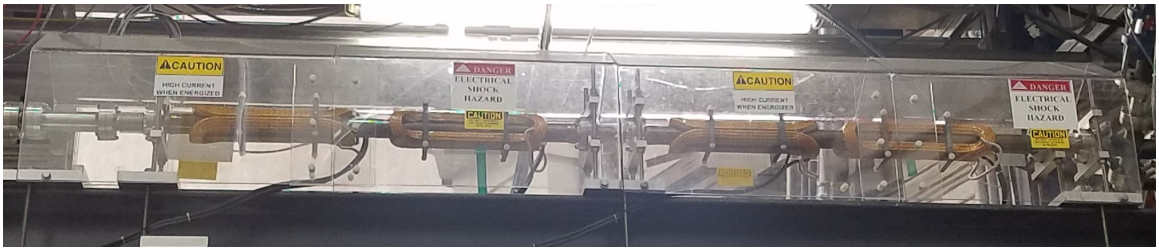

Figure 2.1: The Hall A raster consists of four dipole magnets on the beamline

are introduced sequentially into the path of the beam using a stepper motor. When the beam is incident on a wire, a charge is induced. By determining when each wire is struck by the beam, the experimenter can very accurately determine the position of the beam. This is an invasive measurement.

2.3.2 Raster

The raster is a beamline apparatus in Hall A for spreading the beam onto the target, rather than being at a single point. This is done to prevent localized heating of the target. The raster consists of four dipole magnets, two for steering in the x-direction and two for steering in the y-direction.

Each raster magnet is powered by a triangle wave of different frequencies to minimize harmonics. The horizontal rasters are set to 24.5 kHz and the vertical rasters are set to 25 kHz. When running properly, the x-direction magnets will be synced and the y-direction magnets will be synced. This syncing ensures that the magnets are always working together to create the desired beam spread.

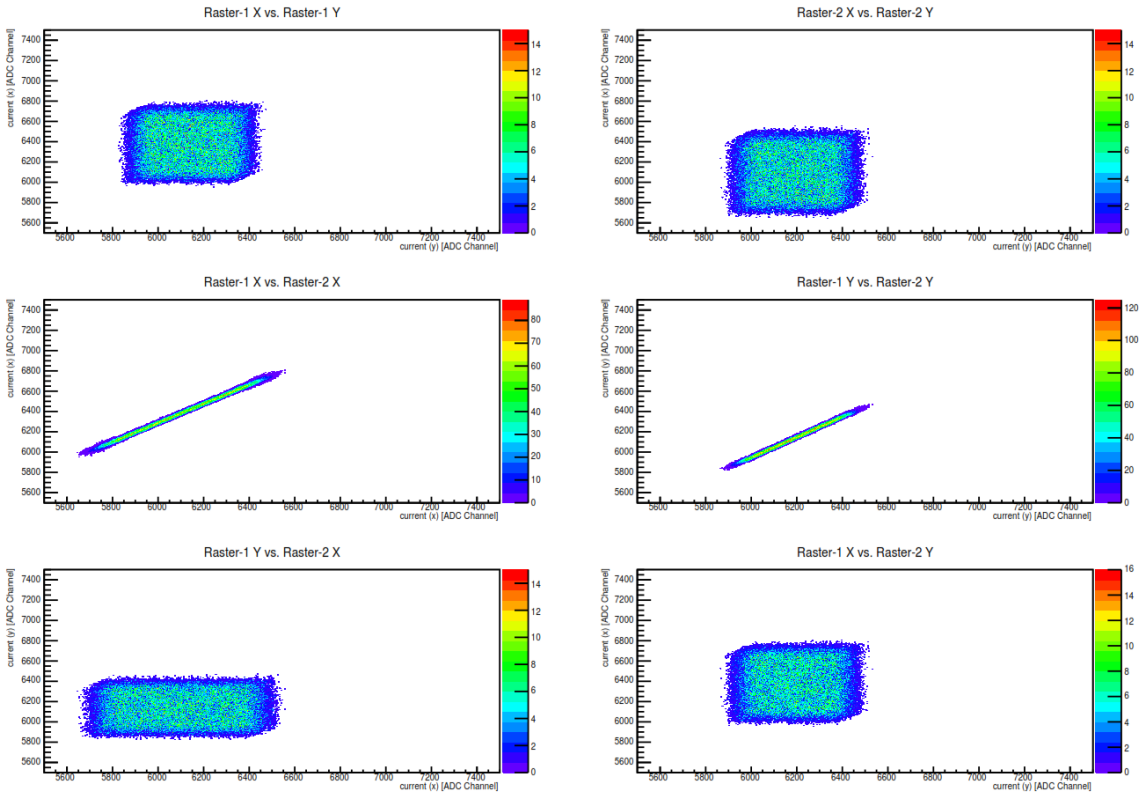

Figure 2.2: The X and Y raster pairs are each synced to produce the maximum kick. The X and Y directions are uncorrelated so that the beam travels uniformly over the target.

2.3.3 Beam Current Monitors

2.4 Tritium Target System

2.4.1 Cell Design

2.4.2 Target Chamber and Ladder

The MARATHON experiment used six different targets for physics. These are

- Tritium
- Deuterium
- Hydrogen
- Helium-3
- Empty Cell
- 25cm Dummy

With the exception of the 25cm Dummy target, all of these targets use the same cell design. The target cells are 25 centimeters long and made of Aluminum 7075. The cells are sealed and utilize conductive cooling to mitigate the risk of a Tritium leak.

In a closed cell, localized beam heating can create a "boiling" effect on the gas. This is seen as a change in the effective density of the target. Experimental time was dedicated to understanding the magnitude of this effect and will be further discussed in section blah.

The 25cm Dummy is comprised of two Aluminum 7075 foils 25cm apart, this is the same material as the other target cells. Each foil is $0.3495 \pm 0.0006\ g/cm^2$ thick, significantly thicker than the cell walls.

In addition to these, we also utilized several solid targets for procedural studies.

- Optics Target - 11 Carbon Foils
- Carbon Hole - A carbon foil with a 2mm diameter hole in the center
- Raster Target - A "straw" for ensuring the beam is not coming in at an angle
- Thick Aluminum - For calibrating the ion chambers
- Single Carbon Foil
- Titanium
- Beryllium Oxide

Chapter 3

Analysis

3.1 Calibration

3.1.1 Raster Calibration

A well calibrated raster will map a raster current to the instantaneous beam position on the target. Accurate beam position data is critical for proper reconstruction of the reaction vertex of physics events. A poorly calibrated horizontal raster will cause poor z-vertex resolution, making it more difficult to subtract the background from target endcaps. A poorly calibrated vertical raster will incorrectly reconstruct event momentum, causing errors in physics analysis.

In Hall A, we have two sets of raster coils working in tandem for the 12 GeV era. Each set of raster coils are synced to ensure that they work together, always steering the beam in the same direction. With this knowledge, the Hall A Analyzer is set up so that the signals from a single raster set are used to determine the beam position. In our case, the analysis code is set up to use the upstream raster coils.

The raster calibration can be thought of as defining a line that maps the raster current (measured in ADC bins) to a position on the target. Each coil will have two calibration values, the slope and intercept of this line. The slope of the line determines the size calibration of the raster coil, the value converts the raster current (in ADC units) to a beam position displaced about the mean beam position. The intercept of the line, in conjunction with the slope, sets this mean beam position.

In the past, these values have been found by assuming that the BPMs accurately reflect the mean position and overall magnitude of the rastered beam. By mapping the mean and extremes of raster current to the mean and extremes of BPM positions, a 1:1 mapping could be quickly achieved. Unfortunately, in the Tritium era of Hall A, we have seen that the BPMs no longer accurately reflect the magnitude of the rastered beam. An explanation of this behavior has not been found. Nevertheless, we must find a new calibration method.

While the BPMs can (and still are) used to determine the mean beam position, we must look for other quantities to calibrate the raster size. The obvious choice is the carbon hole target. The carbon hole is used to set the size during data taking because it is known to have a diameter of 2mm. The hole is visible in the raster spectrum, so we can fit it to determine a size calibration for the raster.

The resolution of reconstructed events does not allow for a hard line between the events originating from the foil and the absence of events in the "hole" region. Events smear across this border suggesting that we ought to use a smooth function to define the edge. I decided to use a radial sigmoid function with a floating "hardness" constant. A sigmoid is a smoothed step function with a constant that determines how hard of a step it is. As shown in Figure 3.1, a sigmoid approaches a step function as the "hardness" constant approaches infinity. This was found to converge[1] and visually appears to fit the hole well. This fitting procedure determines the edge of the hole to be at the position where the value is halfway between the minimum and maximum value of function.

[1]When doing these fits, be sure to the Log Likelihood method

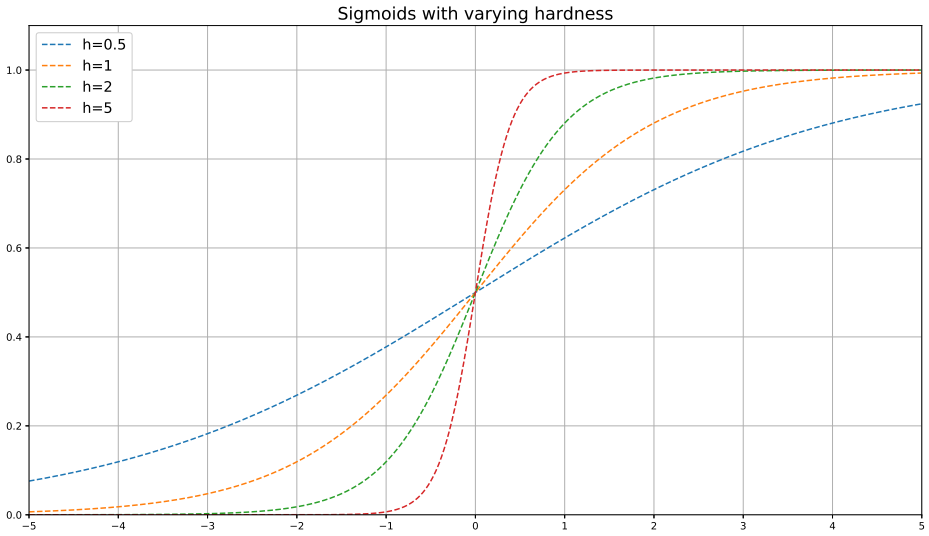

Figure 3.1: A 1 Dimensional Sigmoid Function with Varying Hardness Parameter

The function used is:

$$\frac{[0]}{1+e^{-[5]*\left(([1]*([2]-x))^2+([3]*([4]-y))^2-1\right)}}+[6] \tag{3.1}$$

In this function:

Variable Definitions

[0]	Approximate signal level outside the carbon hole (measured in ADC bins)
[1]	Current (ADC) to size conversion factor for Horizontal Raster
[2]	Horizontal center of the carbon hole in current (ADC) units
[3]	Current (ADC) to size conversion factor for Vertical Raster
[4]	Vertical center of the carbon hole in current (ADC) units
[5]	"Hardness" factor for the sigmoid (approaches a step function as this increases)
[6]	Approximate signal level inside the carbon hole (measured in ADC bins)

Upon further analysis it was determined that the calibration was not good. The fit places the edge of the hole at the zero-crossing of the sigmoid function. Due to smearing from the spectrometer, this is not the "true edge" of the hole.

Proceeding further, we determined that we ought to look at the physics values that the raster calibration affects. For the horizontal rasters, this is the reconstructed z position at the target. For the vertical rasters, this is W^2. By utilizing two "bad" calibrations, we can interpolate (or extrapolate if they were bad in the same direction) to determine the correct calibration.

For the horizontal raster, we use the single carbon foil target and plot the horizontal raster current versus the reconstructed z position. We can then take slices of this plot in horizontal raster current bins and fit the resulting plots with a Gaussian and plot the peaks. With a properly calibrated raster, there should be no correlation between horizontal raster current and reconstructed z. Using two improper horizontal calibrations, we measured the slopes of the correlations. We then interpolated to determine the calibration that would yield a slope of 0.

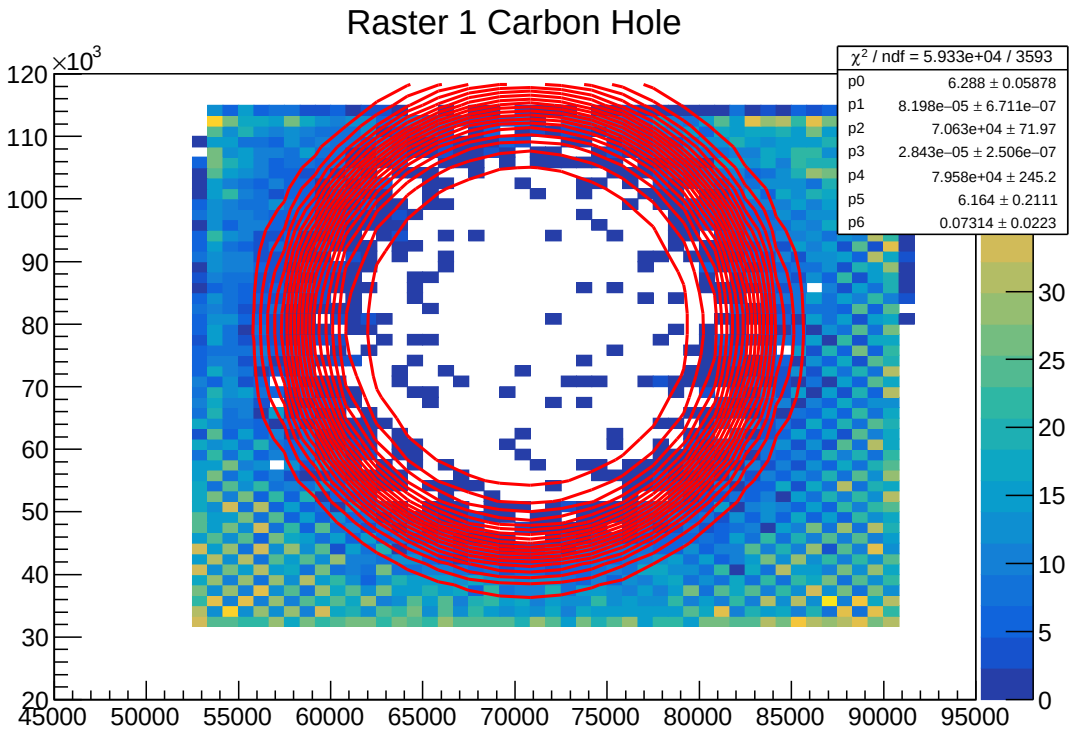

Figure 3.2: Using the radial sigmoid function to fit the hole in the Carbon Hole target. In this plot, the density of red rings is directly correlated to the slope of the function at that point. Where the rings are densest is the 50% position, corresponding to where the fit locates the edge of the hole.

In practice, this does not yield a calibration with a slope of *precisely* zero. This is due to statistical fluctuations in the data around the true correlation line. We attempted to iterate this procedure, but it did not yield significant improvement on the results.

For the vertical raster, we look for a momentum feature that the experiment can see. In the case of many of the Tritium era experiments, the Hydrogen elastic peak was measured. Plotting the vertical raster current versus the W^2 of Hydrogen elastic events, we followed a similar procedure to that of the horizontal raster.

For experiments that do not have an identifiable momentum feature, an approximation of the correct vertical calibration can be found using the horizontal calibration and the sigmoid fit of the carbon hole. Since it is known that the true calibration lies somewhere on the sigmoid above the zero-crossing, we can use the horizontal calibration to determine where that point is. To do this, we determine how many horizontal ADC bins away from center the "true edge" lies using the calibration determined using the z vertex reconstruction (the "true edge" is $1mm$ away from the center). We then evaluate equation 3.1 using this value. Then, equation 3.1 is reversed to determine the vertical ADC bin displacement to yield the same value. Once we have the displacement, a new vertical calibration can be determined. This is an imperfect solution, but ultimately should provide the best calibration possible in the absence of a momentum feature.

Once these methods are used to determine the slope of the raster calibration, we turn our attention back to the BPMs. The BPMs, after calibration with the harp, provide a very accurate reading of the mean beam position at their location in the beamline. This information can then be used to determine the mean position of the

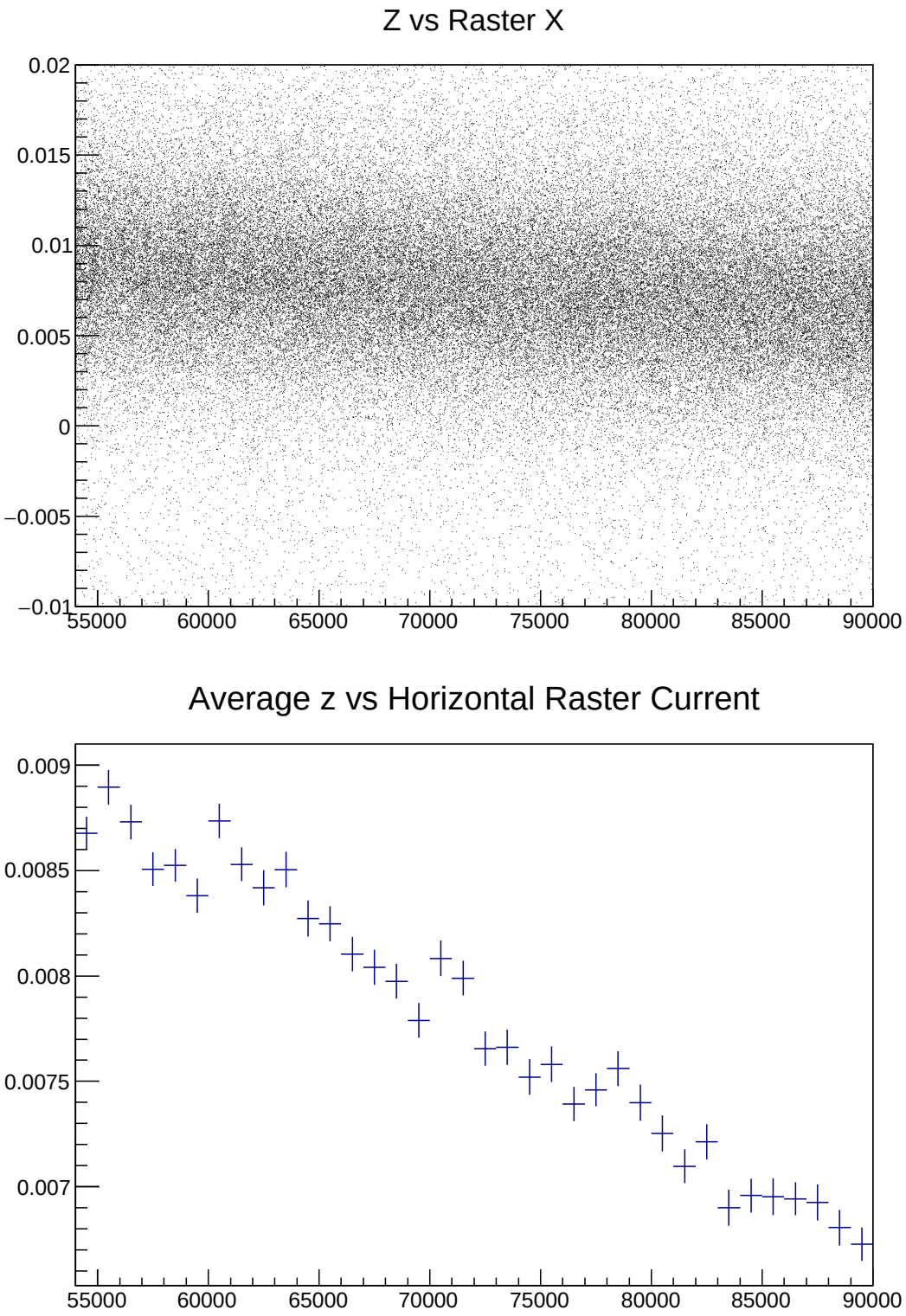

Figure 3.3: Slices in horizontal raster current of the reconstructed z versus raster current plot are fit with a Gaussian. The peaks of the Gaussian are then plot to see the correlation. In the plot of average z, it can be seen that the peak position shifts by over 2mm over the movement of the raster. The carbon foil is only 0.25mm thick.

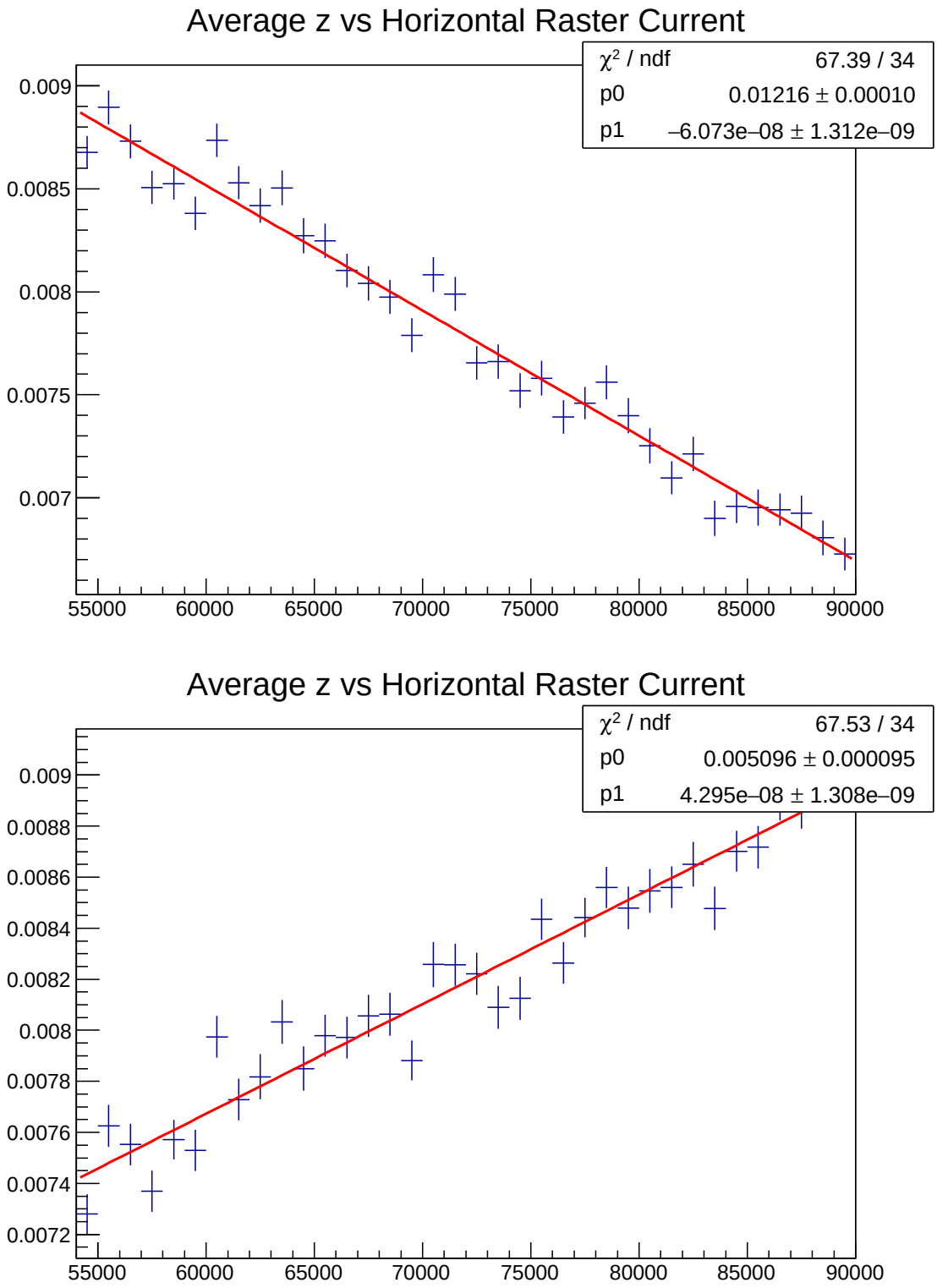

Figure 3.4: Two "bad" calibrations are fit to find the correlation between horizontal raster current and the average x position. Both of these calibrations show a displacement larger than the thickness of the target.

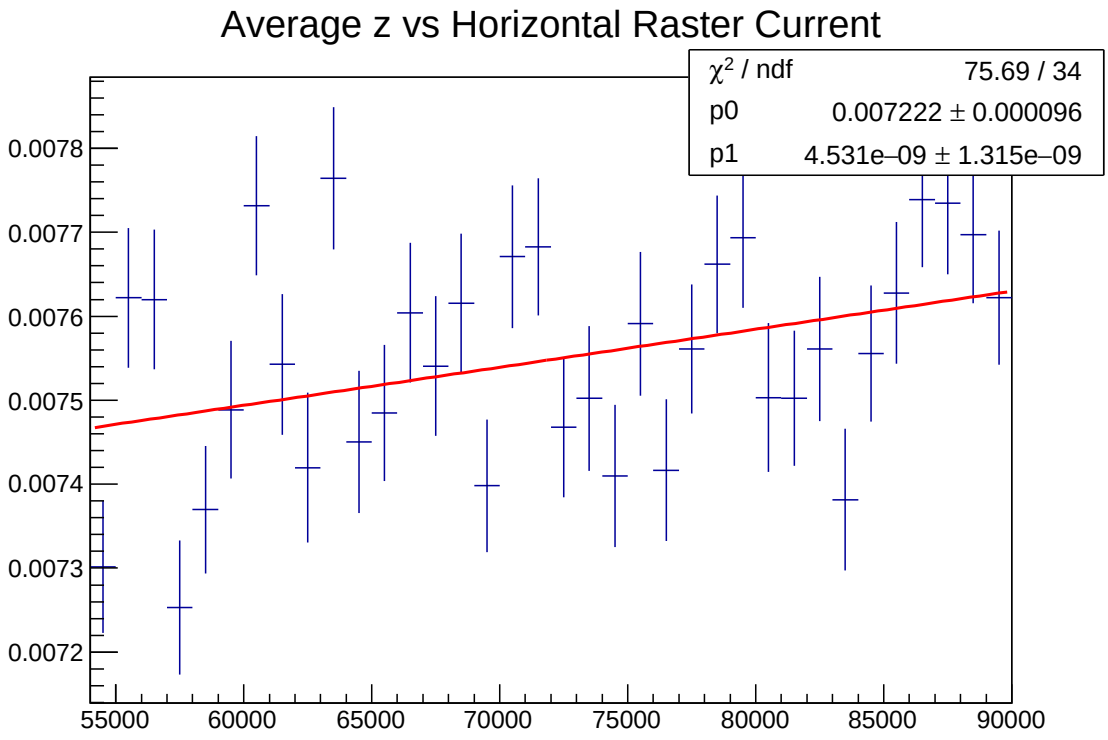

Figure 3.5: Using a linear fit of the correlation between average z and horizontal raster current for two "bad" calibrations, we can interpolate to the correct calibration. Here we can see that the shift is approximately 0.1mm.

beam at the target. To do this, we plot each BPMs position spectrums and determine the mean value. Each spectrum must have its mean determined independently because the BPM readings lag behind events, the position is only accurate when averaged over time. Once we know the mean positions at each BPM, a track through the means can be projected to the mean position at the target.

With the slope of the raster calibrations and a point on the calibration lines (the mean position at the target), we have all the information that we need to determine the raster calibration lines. Using a simple point-slope form, we input the information for each raster and solve for the intercept.

3.2 Analysis

3.2.1 Corrections

Target Boiling

Reference Sheren and Natalie paper.

Localized heating from the beam causes changes to the gas density of the target. The target does not actually boil, but the standard nomenclature for a change in target density is "boiling". By modulating the gas density, the incident beam sees a variable target thickness. This in turn affects the yield calculation.

This effect scales with the current that is on the target. We make this correction run-by-run using the average current during beam-on time during the run. This method was chosen because the average current is near constant over the coarse of a single run and the effect is approximately linear for small deviations in current. It was found that the change in density settles very quickly, so it is unnecessary to take into account beam ramp-up after beam trips.

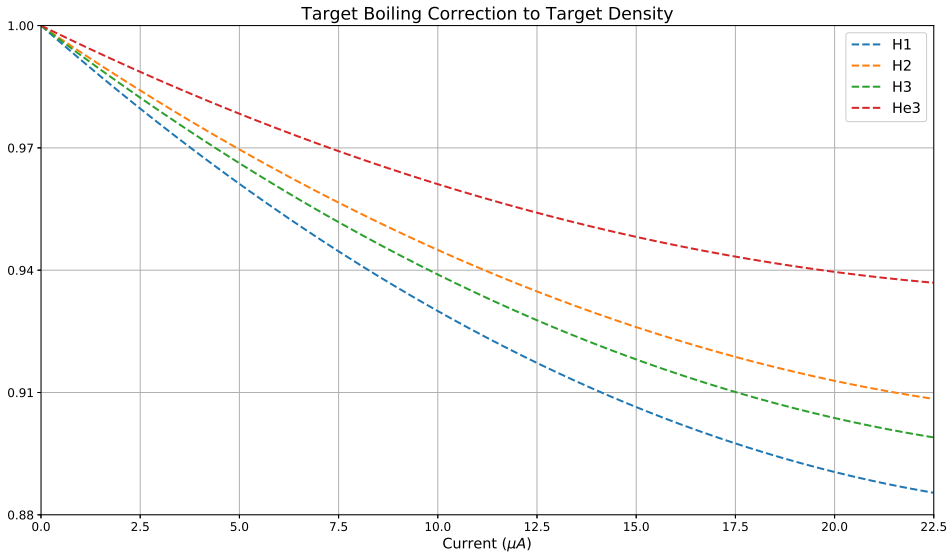

Figure 3.6: Beam heating effects are manifested as a multiplicative correction to the target density

To determine the correction, a dedicated set of runs was taken with the Left HRS spectrometer at 16.8° and 3.1GeV. The data was taken at varying currents in order to assess the affect of the beam current on the normalized yield. By applying nominal event cuts to this data, the normalized yield was calculated.

To determine the density correction, the normalized yields were plotted versus the beam current for that measurement. The data was then fit with a quadratic polynomial. The fit was constrained to require a correction of 1 (no correction) at a current of 0μA.

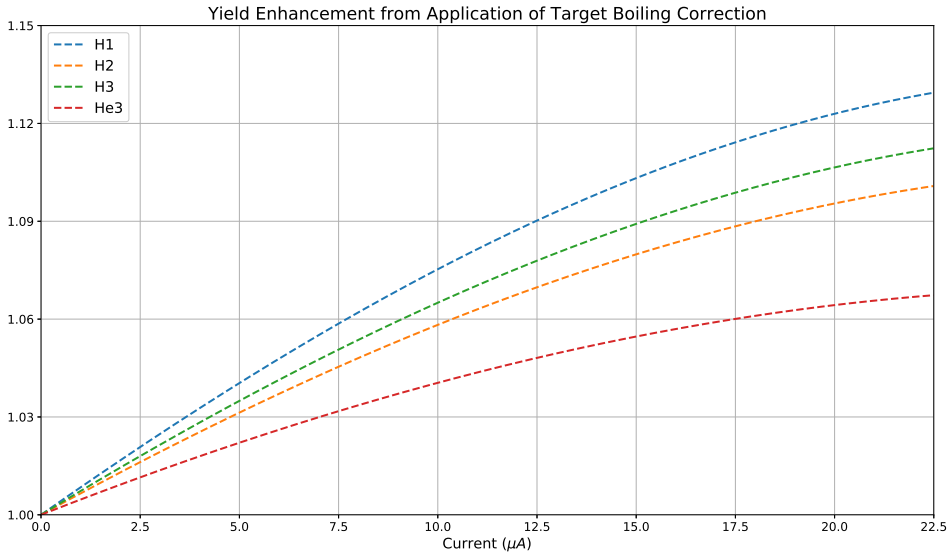

Figure 3.7: Target density corrections cause a multiplicative enhancement to the yield

Target Endcap Contamination

All of our gas targets are stored in an aluminum cell. The thickness of the aluminum greatly exceeds the thickness of the gas and will sometimes contribute background that makes it past our cuts. To determine this contribution, we use an empty cell. The empty cell, being an exact replica of the gas target cells with a vacuum inside, allows us to approximately isolate the contribution of the cell walls to the data.

To determine this contribution, the empty cell is normalized to the target in question. This is done by.....

The data for the target in question and the normalized empty target are then binned in Bjorken x. Dividing the empty cell data by the gas target data then gives an approximation of the fractional contribution of the cell walls to the electron data.

This fractional contribution can be the subtracted from the charge normalized yields to correct for the data coming from the endcaps.

Charge Symmetric Background Subtraction

As an inclusive scattering experiment, we are particularly susceptible to background from charge symmetric processes from the target. To study this background we reversed the polarity of the Left HRS to take positron data at several low Bjorken x kinematics.

Measuring the positron yield allows us to determine the proportion of electron events measured that were a result of pair production. This data was subject to the same cuts that are used on the electron data. It was noted that a significant π^+ contamination occurred for the positron data. The main pion peak was fit and then subtracted from the positron data.

These data were then binned by Bjorken x and fit with an exponential.

Somethin somethin somethin... Provide x of bin and multiply by $1 -$ curve.

Computer Deadtime Correction

Our DAQ unable to be continuously taking data. While we can probabilistically determine the mean time spacing between events, in the real world events can deviate greatly from these means **because statistics**. Sometimes events will occur that are too close in time for our DAQ to record all of them. When deadtime becomes significant, we must correct for it.

An approximation of the computer deadtime was measured with our scalers. The trigger signals generated by the NIM electronics were copied and sent to both the

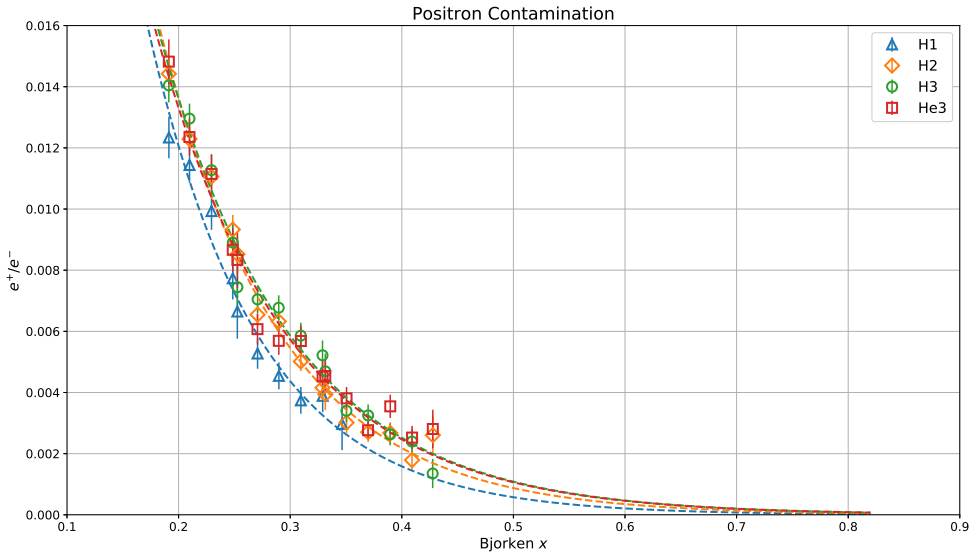

Figure 3.8: Charge symmetric background correction

Trigger Supervisor and a scaler unit. The Trigger Supervisor is subject to the computer deadtime event loss discussed here. The scaler unit simply increments a register when a trigger signal is received. The deadtime is defined on a run-by-run basis as:

$$DT = 1 - \frac{\Sigma \text{Triggers}_{\text{TS}}}{\Sigma \text{Triggers}_{\text{Scaler}}} \tag{3.2}$$

A deadtime correction is applied on a run-by-run basis. The correction is defined as:

$$DT_{\text{correction}} = \frac{1}{1 - DT} \tag{3.3}$$

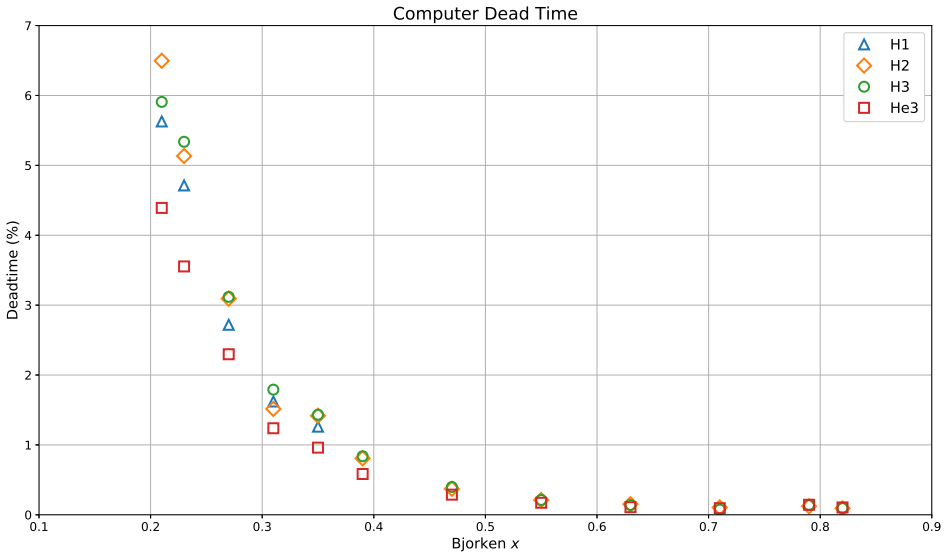

Figure 3.9: Deadtime per kinematic

Radiative Corrections

Isoscalar Corrections

Bin Centering Corrections

Coulomb Corrections

3.2.2 Particle Identification

Chapter 4

Results

Appendix A

Title of Appendix A

References

[1] *Measurement of the F_2^n/F_2^p and d/u ratios and $A = 3$ EMC effect in deep inelastic scattering off the tritium and helium mirror nuclei*, JLab Proposal PR-12-10-103, J. Arrington et al., The JLab MARATHON Collaboration, 2010.

[2] C. E. Carlson, J. R. Hiller and R. J. Holt, Annu. Rev. Nucl. Part. Sci. **47**, 395 (1997).

[3] L. C. Alexa *et al.*, Phys. Rev. Lett. **82**, 1374 (1999); and references therein.

[4] A. Camsonne *et al.*, *Measurement of the ^{4}He charge form factor at large momentum transfers at Jefferson Lab*, to be submitted to Phys. Rev. Lett., May 2013.

[5] A. T. Katramatou, SLAC Report SLAC-NPAS-TN-86-08 (1986).

[6] G. G. Petratos, SLAC Report NPAS-TN-86-07 (1986).

[7] A. T. Katramatou *et al.*, Nucl. Instrum. Meth. **A267**, 448 (1988).

[8] K. Rith. 1997. *Lectures on QCD: Applications*. Berlin, Heidelberg: Springer Berlin Heidelberg. *Quark-Gluon Structure of the Nucleon*; p. 250-346.

[9] F. Halzen, A. Martin. 1984. *Quarks and Leptons: An Introductory Course in Modern Particle Physics*. Wiley.